

Signal Filtering Enabled by Spike Voltage-Dependent Plasticity in Metalloporphyrin-Based Memristors

Zhiyong Wang, Laiyuan Wang, Yiming Wu, Linyi Bian, Masaru Nagai, Ruolin Ju, Linghai Xie,* Haifeng Ling, Qi Li, Hongyu Bian, Mingdong Yi,* Naien Shi, Xiaogang Liu,* and Wei Huang*


Neural systems can selectively filter and memorize spatiotemporal information, thus enabling high-efficient information processing. Emulating such an exquisite biological process in electronic devices is of fundamental importance for developing neuromorphic architectures with efficient in situ edge/parallel computing, and probabilistic inference. Here a novel multifunctional memristor is proposed and demonstrated based on metalloporphyrin/oxide hybrid heterojunction, in which the metalloporphyrin layer allows for dual electronic/ionic transport. Benefiting from the coordination-assisted ionic diffusion, the device exhibits smooth, gradual conductive transitions. It is shown that the memristive characteristics of this hybrid system can be modulated by altering the metal center for desired metal–oxygen bonding energy and oxygen ions migration dynamics. The spike voltage-dependent plasticity stemming from the local/extended movement of oxygen ions under low/high voltage is identified, which permits potentiation and depression under unipolar different positive voltages. As a proof-of-concept demonstration, memristive arrays are further built to emulate the signal filtering function of the biological visual system. This work demonstrates the ionic intelligence feature of metalloporphyrin and paves the way for implementing efficient neural-signal analysis in neuromorphic hardware.

1. Introduction

Synaptic plasticity is a fundamental property of the human brain, which endows the neural network with intelligent information processing that is far superior to the von Neumann architectures.^[1] Multifarious plasticity grants various cortical functions in the human brain, including learning-experience, associative learning, habituation/sensitization, forgetting, probabilistic inference/fault-tolerant, and self-adaptive feature.^[1c,e–h] In particular, plasticity enables computing-in-memory, thereby boosting the signal with cocktail party effect or filter background noise while keeping energy efficiency.^[2] Inspired by this, achieving analogous neuromorphic hardware has attracted considerable attention to pursuing highly efficient information processing in the era of big data.^[3] Recently, based on their operation history-dependent tunable and storable conductive states, memristive devices have been intensively studied to emulate

Z. Wang, L. Wang, L. Bian, R. Ju, L. Xie, H. Ling, M. Yi, N. Shi, W. Huang
 Center for Molecular Systems & Organic Devices (CMSOD)
 Key Laboratory for Organic Electronics and Information Displays &
 Institute of Advanced Materials (IAM)
 Nanjing University of Posts & Telecommunications
 Nanjing 210023, China
 E-mail: iamhxie@njupt.edu.cn; iammdyi@njupt.edu.cn;
 iamwhuang@njtech.edu.cn
 Y. Wu, H. Bian, X. Liu
 Department of Chemistry
 National University of Singapore
 Singapore 117543, Singapore
 E-mail: chmlx@nus.edu.sg
 Y. Wu, X. Liu
 Institute of Materials Research and Engineering
 Agency for Science
 Technology and Research
 Singapore 138634, Singapore

M. Nagai, W. Huang
 Key Laboratory of Flexible Electronics (KLOFE) & Institute of Advanced
 Materials (IAM)
 Nanjing Tech University (NanjingTech)
 Nanjing 211816, China
 L. Xie, W. Huang
 Frontiers Science Center for Flexible Electronics
 Xi'an Institute of Flexible Electronics (IFE) and Xi'an Institute of
 Biomedical Materials & Engineering
 Northwestern Polytechnical University
 Xi'an 710072, China
 Q. Li
 Physical Science Division
 IBM Thomas J. Watson Research Center
 1101 Kitchawan Rd, Yorktown Heights, NY 10598, USA
 X. Liu
 Joint School of National University of Singapore and Tianjin
 University International Campus of Tianjin University
 Fuzhou 350207, China

 The ORCID identification number(s) for the author(s) of this article can be found under <https://doi.org/10.1002/adma.202104370>.

DOI: 10.1002/adma.202104370

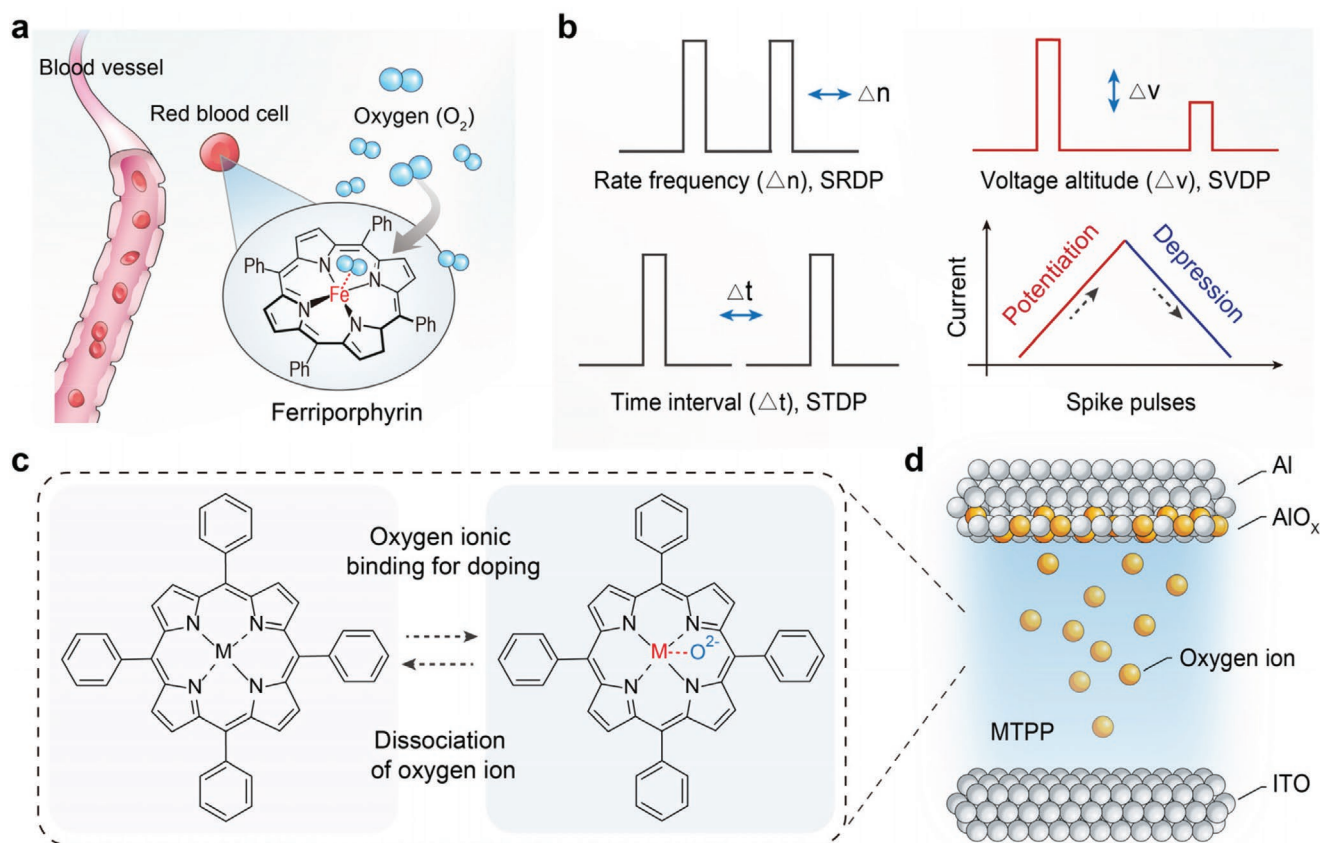


Figure 1. Concept of a molecular memristor with SVDP. a) Bioinspired material selection. In vertebrate red blood cells, ferriporphyrin (a component of hemoglobin) can reversibly bind and dissociate oxygen, thus allowing continuous oxygen delivery. b) Visual summary of plasticity in synapses and memristors. The proposed SVDP with unipolar plasticity allows selective depression or potentiation by programming positive-voltage spikes with fixed frequency and interval. c) Schematic of ionic migration among MTPP molecules. M = Zn, Ni, Co, Fe-Cl, and 2H represent ZnTPP, NiTPP, CoTPP, FeTPPCL, and TPP, respectively. d) Configuration of ITO/MTPP/ AlO_x /Al device. The drift of internal O^{2-} dictates the switching behavior.

synaptic plasticity and construct artificial synapse arrays.^[3,4] Although their key performance is comparable with that of synapses,^[5] precisely controllable and highly repeatable ionic processes in the synapse,^[6] which are critical for delicately emulating plasticity, remain unattainable.

From a function perspective, the combination of pathway-specific gating capacity with the multiple depression plasticity of synapses enables human brains to selectively focus on specific visual targets in complex, real-world environments and filter other perceivable but irrelevant information when performing visual recognition tasks.^[7] In contrast, current filtering units in artificial cognitive systems typically rely on fuzzy set extensions or low-pass filtering and suffer from high power consumption and complex configurations, which are fundamentally different from how the brain processes information.^[8] These inspire us to leverage new memristor devices that are analogous to the brain to process noise or off-pathway signal filtering for future neural signal analysis in neuromorphic computing systems.

Herein, inspired by the mechanism of voltage-gated ion channels and oxygen delivery in biological processes (Figure 1a), a memristor based on hybrid heterojunction metalloporphyrin (MTPP)/ AlO_x was investigated, which employed MTPP as molecular multimedia for oxygen transport. The

measured electrical and microstructure data exclude the effect of metallization or filament, revealing that coordination-assisted modulation contributes to the memristive characteristics. Theoretical calculations and metal-dependent memristive behaviors suggest that the metal–oxygen (M–O) binding energy and the resultant device properties can be delicately tuned by changing the MTPP species. Importantly, unipolar spike voltage-dependent plasticity (SVDP) generated by the interfacial counterbalance between ionic Coulomb forces and the external electric field was demonstrated. This behavior is fundamentally different from spike-rate-dependent plasticity (SRDP), spike-timing-dependent plasticity (STDP), and conventional bipolar SVDP, which typically require an extra algorithm to guide the passive operation/execution. By programming positive-voltage spikes with fixed frequency and interval (Figure 1b), we achieved neuromorphic systems with signal filtering, closely resembling human visual recognition systems.

2. Results

The proof-of-concept memristive devices are constructed as ITO/ZnTPP (≈ 25 nm)/ AlO_x (≈ 7 nm)/Al (Figure 1c,d). The non-stoichiometric AlO_x layer with oxygen vacancies is employed

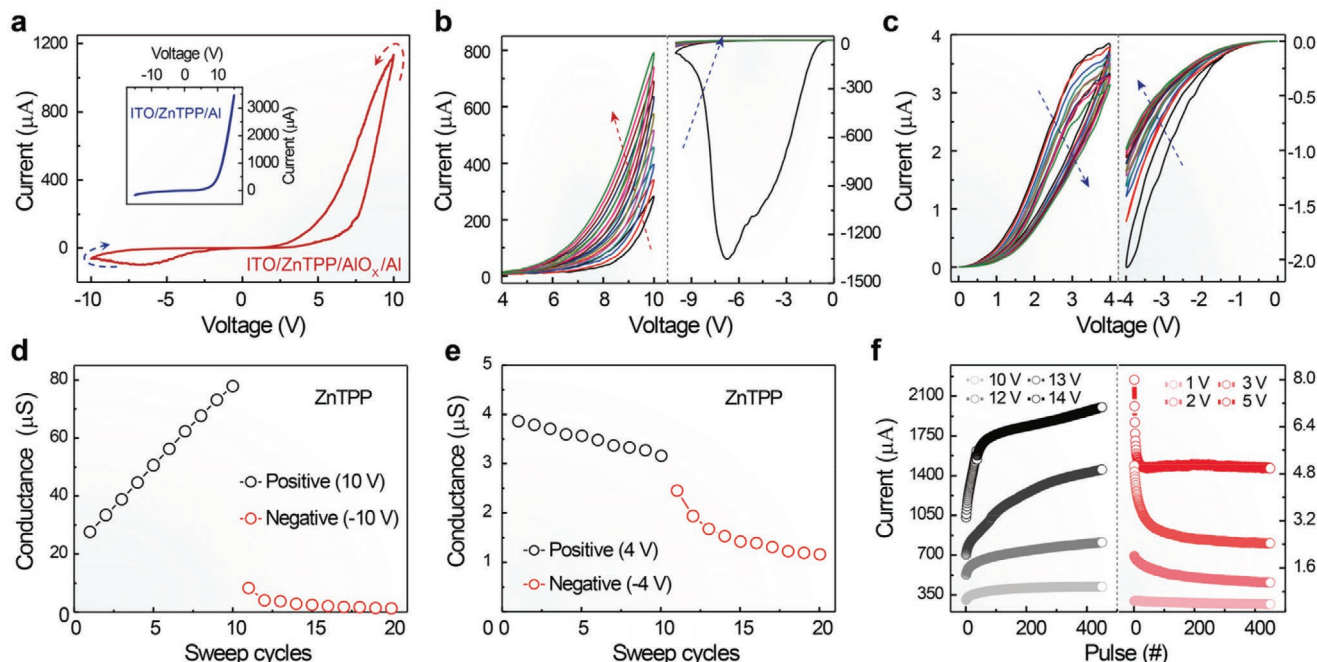


Figure 2. Electrical characteristics of ZnTPP/AlO_x device. a) Typical *I*-*V* curve, which shows a pinched hysteresis loop at positive and negative bias voltages. The voltage was swept from zero to 10 (−10) V, then back to zero. Inset shows the device performance of the ITO/ZnTPP/Al memristor. The absence of AlO_x enables the device to transport only electrons/holes, resulting in a distinct diode feature. b,c) Hysteretic *I*-*V* loops of the ZnTPP/AlO_x devices during 10 voltage-sweep cycles of 0 → 10/−10 V → 0 and 0 → 4/−4 V → 0, respectively. The device conductivity continuously increases (decreases) during the positive (negative) voltage sweeps. d,e) Conductance versus sweep cycles in potentiation and depression, respectively. f) Voltage-dependent endurance-cycling performance test. Bias stimuli above ($V_{\text{high}} = 10, 12, 13$, or 14 V) and below ($V_{\text{low}} = 1, 2, 3$, or 5 V) the critical value were applied to two fresh devices, respectively. The applied voltage pulse consists of two segments: a V_{high} or V_{low} /100 ms programming voltage and a 0.5 V/100 ms read voltage.

as an oxygen ions (O^{2-}) reservoir and a current limiter to suppress the metallization of electrodes.^[9] As indicated by the energy diagram (Figure S1, Supporting Information), the device preferentially transports holes, and the p-type ZnTPP layer is expected to modulate the conduction of mixed O^{2-} ions and electrons, thus triggering memristive switching.^[9,10] As shown in Figure 2a, the measured current–voltage (*I*-*V*) curve ranging from +10 to −10 V displays a typical “figure-8” pinched hysteresis loop. In contrast, no memristive hysteresis was observed in the cyclic sweeping curves of the ITO/ZnTPP/Al and ITO/AlO_x (≈ 7 or ≈ 36 nm)/Al devices (Figure 2a, inset; Figure S2, Supporting Information), indicating that the hybrid heterojunction dominates the memristive behavior.

The gradually changed conductive states of hysteresis loops reveal that the memristive characteristics in the ZnTPP/AlO_x device are regulated by ionic movement (in contrast to local filamentary-determined conduction in insulators). The potentiation and depression behaviors of the ZnTPP/AlO_x device were examined in bipolar sweeping mode (Figure 2b, 10 cycles in the 0 → +10 V range scanned at 0.01 V s^{-1} , followed by 10 cycles in the 0 → −10 V range scanned at 0.01 V s^{-1}). The ultimate currents of the ten positive and negative sweep cycles show marked variations ranging from ≈ 270 to $778 \mu\text{A}$ and from -80 to $-10 \mu\text{A}$, respectively. The negative differential resistance (NDR) appeared at -6.7 V during the first RESET sweep. Significantly, smooth *I*-*V* curves are repeatable (Figure S3, Supporting Information), making hybrid ZnTPP/AlO_x a suitable

model for robust neuromorphic computing. It should be noted that the device remained fully functional after one year of storage under ambient conditions (Figure S4, Supporting Information), illustrating its potential for environmentally robust electronic applications.^[11] In addition, to evaluate device-to-device reproducibility, we analyzed the distribution of ON/OFF state resistances in 50 devices. All measurements showed comparable resistive switching and batch-to-batch performance with normal distribution of ON/OFF state resistances (Figure S5, Supporting Information).

I-*V* characteristics were further investigated by repeating low-voltage sweep cycles of $0 \leftrightarrow +4 \text{ V} \leftrightarrow -4 \text{ V}$ based on a fresh device (Figure 2c). Interestingly, both positive and negative directions show clockwise hysteresis loops with ultimate currents decreasing from about 3 to $3.8 \mu\text{A}$ and from -2 to $-0.96 \mu\text{A}$, respectively. This indicates that the low voltage can induce a continuous transition to a higher resistance state. Figure S6a (Supporting Information) displays the fitting results of the first voltage loop in $0 \leftrightarrow +10 \text{ V}$ and $0 \leftrightarrow +4 \text{ V}$, revealing that the device follows the space charge limited current (SCLC) model. The response current of the device converts from a low exponential SCLC (fit slope of about 2) to a high exponential SCLC (the fit slope greater than 6) as the voltage increases. Note that only with a high voltage, sufficient charges can occupy deep traps. In contrast, the low voltage sweeps of $0 \leftrightarrow +4$ lead to the retentive trapping charges, thus enabling a clockwise hysteresis and a memory charge in the new scanning voltage

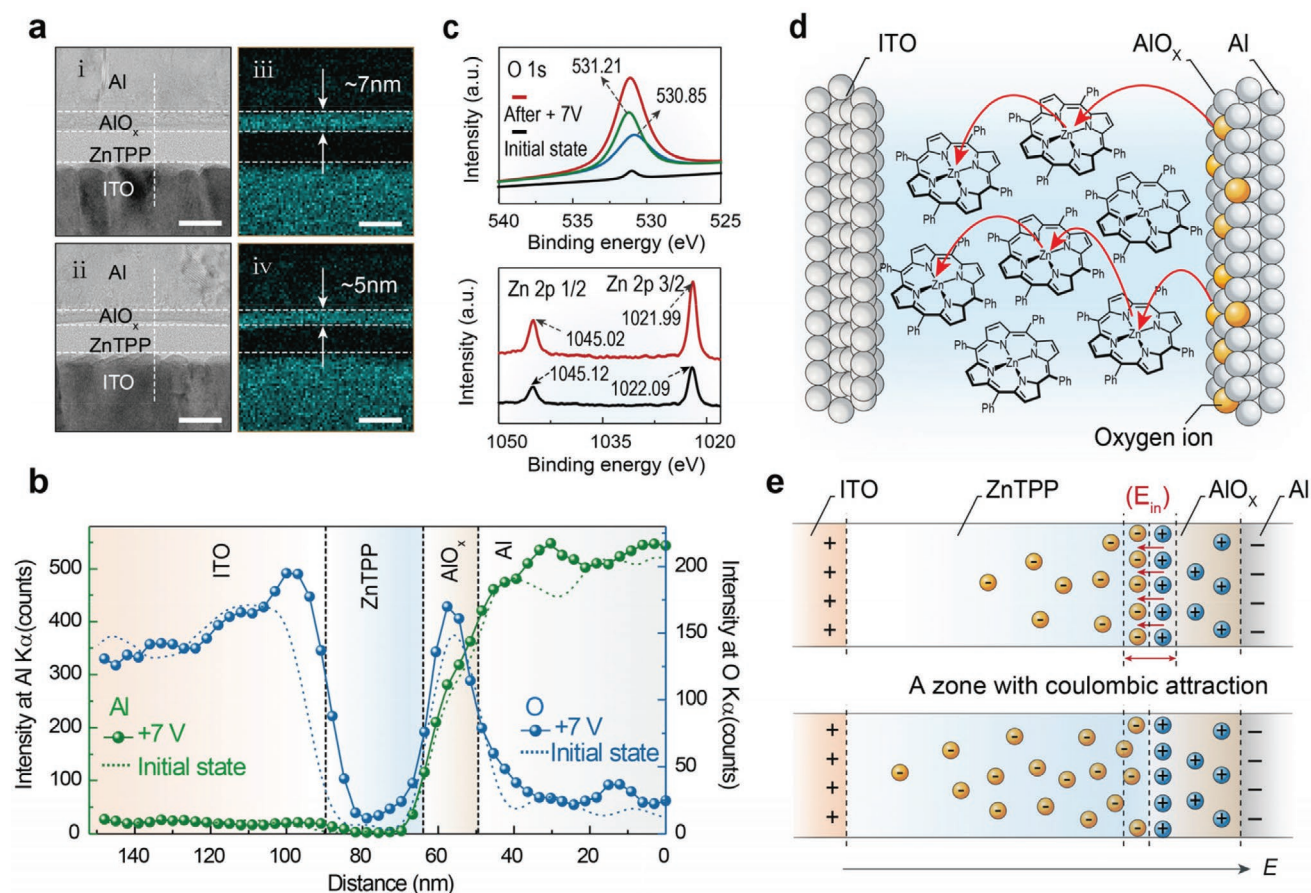


Figure 3. STEM-EDX characterization and mechanism of the ZnTPP/AlO_x devices. a) STEM images and corresponding STEM-EDX elemental mapping of O (blue) in the virgin (i and iii) and energized (ii and iv) samples under a voltage bias of +7 V. b) Elemental line-scanning profiles from the Al to ITO sides (marked by white lines in (a) (i and ii)). c) Typical high-resolution O 1s and Zn 2p XPS spectra. Data were collected from the pristine state after electrode polarization. d) Schematic of the proposed model. ZnTPP regulates memristive behavior by functioning as an ionic/electronic media. e) Schematic of O²⁻ redistribution under a weak (upper panel) and intense (bottom panel) external electric field.

loops. Therefore, the potentiation and depression in ZnTPP/AlO_x memristors can be selectively operated at a unipolar voltage (e.g., 10 V for potentiation and 4 V for depression; see Figure 2d,e and Figure S6b,c, Supporting Information). Such features distinguish SVDP from other synaptic plasticity forms, such as SRDP and STDP, rendering the device relatively independent of signal processing under a fixed rate frequency and time interval. To further confirm the SVDP behaviors, we carried out additional measurements in biasing modes (Figure 2f). We found that the stimulus-response for a fresh device exhibited an inverse trend with a critical value of ≈ 6 –7 V. More specifically, bias stimuli above (10, 12, 13, or 14 V) and below (1, 2, 3, or 5 V) the critical value induce potentiation and depression, respectively. Hence, our device can selectively perform potentiation and depression of input signals, resembling action potentials in neurons. This behavior is reproducible, making the ZnTPP/AlO_x device a promising candidate for constructing artificial neural hardware.

To shed light on the underlying mechanism of plasticity in the ZnTPP/AlO_x devices, we performed a series of structural and stoichiometric characterizations with theoretical simulations and device evaluations. The measurements as

a function of device area reveal a monotonic increase in current (increasing from ≈ 74 to ≈ 1500 μA at high resistance state (HRS) and from ≈ 454 to ≈ 4048 μA at low resistance state (LRS)) with an increase in the device area from 5×10^3 to 5×10^5 μm^2 (Figure S7, Supporting Information). As evidence of the memorization of stimulus-dependent ion migration, the increasing scan strides (v_{st}), which ranged from 0.01 to 5 V s^{-1} , significantly reduced the overall conductive level (from ≈ 1112 to ≈ 10 μA at LRS, and from ≈ 51 to 16 μA at HRS) and the hysteresis area (from ≈ 54.9 to 2.0 $\text{V } \mu\text{A cm}^{-2}$) (Figure S8, Supporting Information). These results suggest that device behaviors with the SVDP feature are dominated by homogeneous ionic migration rather than local filamentary conduction.^[12] Conductive filaments can also be excluded by the cross-sectional scanning transmission microscopy and energy-dispersive X-ray (STEM-EDX) analyses of the memristor devices (Figure 3a,c; Figures S9 and S10, Supporting Information). After bias polarity at +7 V, the oxygen component in ZnTPP/AlO_x devices was redistributed in ZnTPP and AlO_x layers. Notably, the thickness of the AlO_x layer decreased from ≈ 7 to ≈ 5 nm, suggesting the partial reduction of Al³⁺ to Al and the departure of oxygen at the AlO_x/Al interface (Figure 3a). The cross-sectional line-scanning

profiles of O and Al in Figure 3b demonstrate that the O content (C) was markedly enriched throughout the ZnTPP film after applying the bias, either at the ZnTPP/ITO interface ($\text{In}_{\text{bottom}}$) ($C_0/C_{+7} = 48.5/134.4$) or at the $\text{AlO}_x/\text{ZnTPP}$ boundary (In_{top}) ($C_0/C_{+7} = 51.5/61.4$), whereas the Al profile remained consistent. The underlying interaction between ZnTPP molecules and mobile O^{2-} was further investigated by X-ray photoelectron spectroscopy (XPS) (Figure 3c; Figure S11, Supporting Information). The greatly enhanced O 1s signals at 530.85 (charged ionic oxygen species (O^{2-}/O^-) bonded with Zn^{2+}) and 531.21 eV (free O^{2-} in the ZnTPP matrix) demonstrates that the bias induces the injection of O^{2-} into the ZnTPP layer.^[13] The Zn 2p spectrum presents a blue shift (100 meV) after electrical stimulation (Figure 3c), arising from the formation of coordination bonds between Zn^{2+} and O^{2-} . Such coordination bonds can finely regulate the O^{2-} distribution and migration, superior to the random and uncontrollable ion diffusion in the thus-far reported memristive media.^[14]

To gain insight into the M–O interactions, we further examined the metal-atom effect of MTPP ($M = \text{Zn}/\text{Ni}/\text{Co}/\text{Fe}/2\text{H}$) on the memristive behavior (Figure S12, Supporting Information), which are summarized in Tables S1 and S2 in the Supporting Information. We observed that the initial conductance, conductance saturation, and change range largely rely on the type of MTPP, because different MTPPs possess different M–O bonding energies. Thus, the O^{2-} migration can be identified as a hopping process through reversible binding and dissociation (Figure 3d). Such O^{2-} kinetics in the MTPP matrix can be described by the Arrhenius equation $\nu = \nu_0 \exp[-(E_{\text{M-O}} - eqa/2)/k_{\text{B}}T]$, where $E_{\text{M-O}}$ is the M–O bond energy, ν is the escape frequency under the applied voltage, ν_0 is the attempt-to-escape frequency, a denotes the average migration step, q is the charge of O^{2-} , k_{B} is the Boltzmann constant, and T is the temperature.^[15] In this context, higher M–O bond energy gives rise to a lower concentration and migration rate of O^{2-} in the MTPP layer. These results verify the significant role of the coordination bond in modulating memristive behaviors while offering intriguing opportunities to develop versatile neuromorphic circuits using MTPP/ AlO_x memristors with tailorable functionalities.

A general model for memristive switching behaviors is proposed (Figure 3d,e). Typically, an applied voltage above the threshold will switch the device to a conductance state limited by the AlO_x layer. This means that sufficient electric field (\vec{E}_{ext}) across the device can attract O^{2-} from the AlO_x reservoir to the ZnTPP matrix. Those negatively charged ions would then bind immediately to ZnTPP molecules through M–O coordination. The calculated $E_{\text{Zn-O}}$ is as low as -1.866 eV. Therefore, mobile O^{2-} can successively hop from one ZnTPP molecule to another through binding and dissociation. The resultant redistribution of the O^{2-} enables a partial collapse of the Schottky-like barrier close to the ZnTPP/ITO interface, thus increasing device conductivity (set to LRS) (Figure S13a,b, Supporting Information).^[1e,16] The retraced sweep further reduces the Schottky-like barrier due to the more effective injection and movement of the O^{2-} , thereby the device is maintained in LRS. Therefore, the switching is essentially nonlinear, which is fundamentally different from the filamentary conduction model. During the following cycles, the iterative effect of the mobile

O^{2-} supports new hysteresis loops with continuous increasing current. In the opposite case, the superposition of the \vec{E}_{ext} -energized ion migration and concentration gradient-enabled diffusion accelerates the retreat of the O^{2-} toward the Al electrode (corresponding to the rapidly increasing current before ≈ -6.7 V) until neutralization by positively charged vacancies or reenters the AlO_x layer via self-limiting oxidation (accounting for the appearance of NDR). The device is then switched OFF as the original ion distribution and Schottky-like barrier are recovered, leading to the memristive characteristics of asymmetrical and gradual resistance changes (Figure S13c,d, Supporting Information).

In contrast, when ZnTPP/ AlO_x devices are operated below the critical voltage, the resulting weak \vec{E}_{ext} cannot effectively influence either O^{2-} injection or movement, which can be respectively ascribed to the Coulombic force between Al^{3+} and O^{2-} and M–O coordination^[1e,17]. As a result, the restrained O^{2-} will progressively accumulate near their equilibrium positions or ZnTPP/ AlO_x interface, and the inverse internal electric field (\vec{E}_{in}) is then established to weaken \vec{E}_{ext} .^[18] In this context, the prolonged weak stimuli tend to enhance \vec{E}_{in} to neutralize \vec{E}_{ext} and induce a degenerative conductive state.

To estimate the potential of our devices in constructing neuromorphic hardware, paradigmatic ZnTPP memristors, which feature a wide range and high density of intermediate states available for computation, are exploited to emulate multiple synaptic functions (e.g., short-term memory (STM)/long-term memory (LTM), “learning–forgetting–relearning” behaviors and visual activity-dependent memory consolidation) by applying specific programming stimuli (Figures S14–S16, Supporting Information). All synaptic responses remained smooth and exhibited gradual changes under long-term, repeated stimulation with different pulse numbers, intervals, and intensities, demonstrating the superiority of coordination-assisted ion migration and consolidation for neuromorphic emulation.

Figure 4a shows the working process of visual recognition systems in the human brain. As a proof-of-concept demonstration, we then emulate the information filtering and memorizing based on the unipolar SVDP feature of MTPP/oxide memristors.^[19] Toward this end, we conducted a validation study using three 8×8 ZnTPP memristor arrays. In our design, the black and violet arrays of the word “Hi” represent the input image stimulation and the memorized electrical pattern, respectively. Assuming sufficient conversion of the photonic signals into electrical signals, the graphic word “Hi” with and without background interference was repeatedly inputted to the memristor array. Meanwhile, the filtering capability of the array was evaluated. In the commonly emulated case 2 without background (Figure 4b), only memristor pixels corresponding to the word were triggered with stimulations ($V_{\text{target}} = 10$ V, $W = 100$ ms, $T = 100$ ms). In this context, a certain number of image stimuli was inputted, and the graphic word “Hi” was memorized and consolidated by a continuous increase of conductance from 30.7 to 66.7 μS (Figure S17, Supporting Information). Figure 4c presents two contrasting cases that affirm the superiority of SVDP in the signal filtering process. Analogous to the biological visual nervous system, the array retained a residual impression of signals that were presented earlier, mimicking the persistence of vision. In case 3,

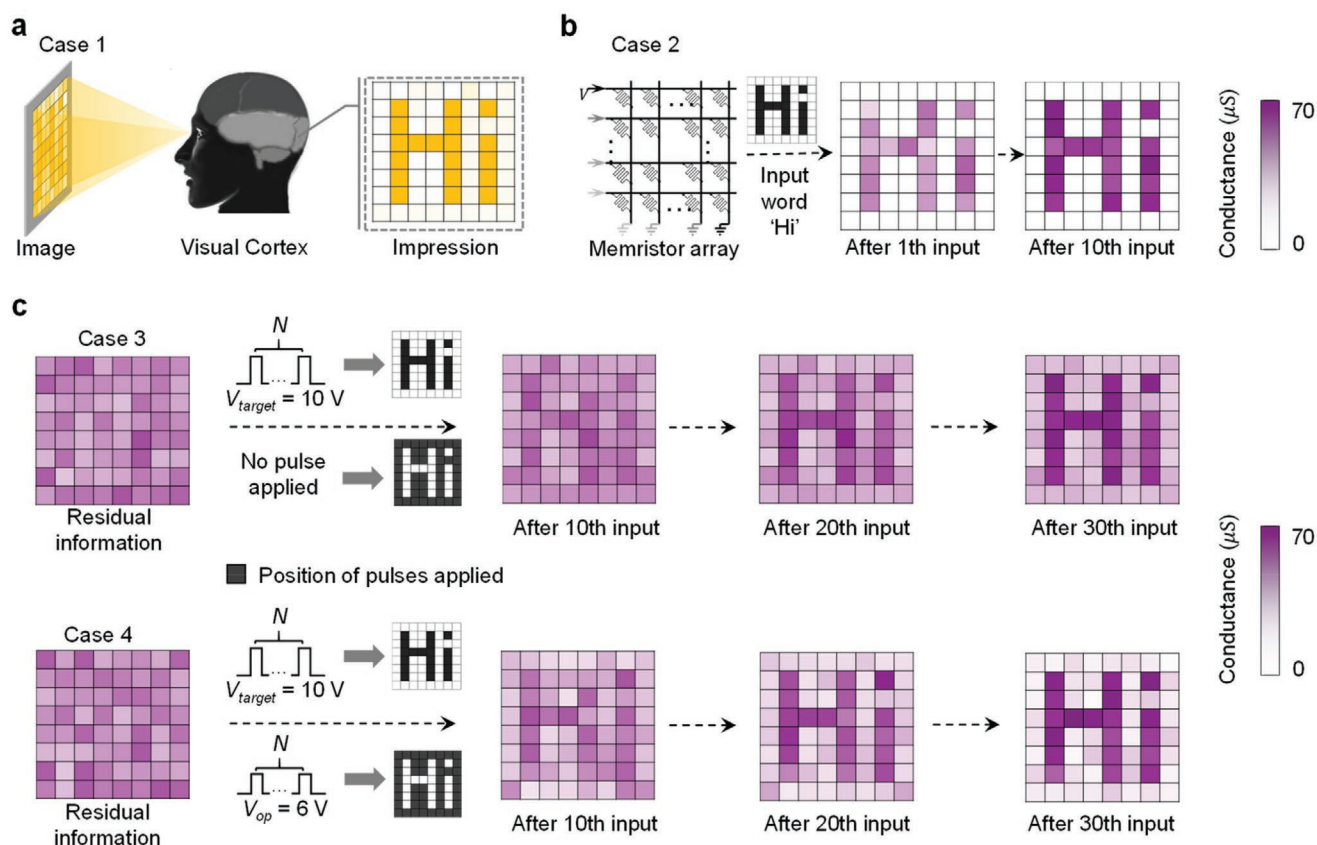


Figure 4. Proof-of-principle design of SVDP-based filtering with unipolar plasticity. a) Working process of visual recognition systems in the human brain. Photonic signals are converted into an electric signal, and background or off-pathway signal is efficiently filtered by the neuron-synapse network. b) Visualizations of the memorizing processes in an ideal case. The response of the devices at the position corresponding to the word ‘Hi’ recorded during the applying of ten stimulation pulses ($V = 10$ V, $W = 100$ ms, $T = 100$ ms). c) Off-pathway signal filtering with and without the SVDP mode. Each pixel represents a single memristor. Initially, all memristive pixels were inspired to a specific conductive state (≈ 31.8 μ S) as residual background information. The applied pulse stimuli and the conductance in the pixels are shown in Figures S17 and S18 (Supporting Information). The pixels of target ‘Hi’ in both case 3 and case 4 were applied with 30 spiking pulses ($V_{\text{target}} = 10$ V, $W = 100$ ms, $T = 100$ ms). Subsequently, the processing without any positive/negative pulse bias voltage program at the off-pathway pixels in case 3, while the off-pathway pixels were applied with 30 spiking pulses ($V_{\text{op}} = 6$ V, $W = 100$ ms, $T_1 = 100$ ms) in case 4 that represents the real biological situation. The changing conductance values in each pixel were recorded at a read voltage of 1 V.

only the pixels of target “Hi” were applied with pulse stimuli ($V_{\text{target}} = 10$ V, $W = 100$ ms, $T = 100$ ms, and $N = 30$). Thus the off-pathway signal filtering relies only on spontaneous decay that represents one noneffective selection. After 30 inputs, the impression level of the pixels of target “Hi” was gradually enhanced from 31.5 to 59.6 μ S, whereas the off-pathway pixels spontaneously relaxed to 18.4 μ S. In contrast, the target “Hi” pixels were operated with 30 identical inputs in Case 4, but the off-pathway pixels were applied with pulse stimuli ($V_{\text{op}} = 6$ V, $W = 100$ ms, $T_1 = 100$ ms, $N = 30$) (Figure S17, Supporting Information). This case more closely represents the real biological situation than the other cases. The changing conductance values in each pixel are shown in Figures S17 and S18 (Supporting Information). As expected, the impression of the word “Hi” in Case 4 changed from 32.1 to 58.0 μ S, whereas the surrounding background information was considerably weakened to ≈ 7.4 μ S. Consequently, the target signal-to-off-pathway contrast ratio of Case 4 filtered by unipolar SVDP was ≈ 8 , far beyond that of Case 3. This demonstrates that the

newly developed unipolar SVDP allows signal filtering to be performed more efficiently, thereby holding the potential for developing high-performance visual recognition systems.

3. Conclusions

In conclusion, we have demonstrated unprecedented MTPP/oxide hybrid memristors with voltage-regulated potentiation and depression behavior. Coordination-regulated ionic dynamics in the memristors were unveiled by STEM-EDS and XPS measurements. The coordination sites of MTPP molecules as a molecular multimedia can regulate oxygen migration, enabling the as-fabricated devices to exhibit smooth, gradually changing memristive responses with durative characteristics. Additionally, the electrical properties of the memristors can be finely modulated by varying the metal constituents. Further, we show that the MTPP/oxide memristors exhibit SVDP behaviors, thus ensuring a signal filtering function. Our studies present a

new type of platform for realizing efficient neural-signal analysis in neuromorphic hardware. It should be noted that further experiments are required to understand the influence of device area, as well as the thickness and morphology of MTPP and AlO_x layers on the device performance, such as power operation, operational voltage, data retention, and endurance. Moreover, the development of hybrid memristor devices with a molecular design approach will not only expand the range of applications but also will advance neuromorphic circuits with memristors as programmable building blocks.

4. Experimental Section

Device Fabrication: Devices were fabricated on commercial ITO-coated 3×3 cm glass substrates with a sheet resistance of $\approx 10 \Omega \text{ sq}^{-1}$. The etched ITO acts as the bottom electrode, and the area of the memristor device is 0.01 mm^2 , as defined by 0.1-mm -wide ITO stripes crossed over by 0.1-mm -wide top Al stripes. Substrates were washed in an ultrasonic bath with acetone, ethanol, and deionized water for 10 min each and then dried in a vacuum oven at 120°C for 30 min. MTPP (5,10,15,20-tetraphenyl-21H,23H-porphyrin zinc(II), ZnTPP; 5,10,15,20-tetraphenyl-21H,23H-porphyrin nickel(II), NiTPP; 5,10,15,20-tetraphenyl-21H,23H-porphyrin cobalt(II), CoTPP; 5,10,15,20-tetraphenyl-21H,23H-porphyrin iron(III) chloride, FeTPPCL; and 5,10,15,20-tetraphenyl-21H,23H-porphyrin, TPP) were obtained from Sigma Aldrich without further purification. MTPP films with a thickness of $\approx 25 \text{ nm}$ were first grown using a thermal vacuum method with an evaporation growth rate of $\approx 0.3 \text{ \AA s}^{-1}$. The film thickness was measured by employing a Step Profiler and verified using STEM. AlO_x films were then fabricated at $\approx 10^{-4}$ Torr using a slow evaporation method with a rate of $0.1\text{--}0.3 \text{ \AA s}^{-1}$, ensuring spontaneous oxidation of Al.^[20] That process resulted in an AlO_x layer ($\approx 7 \text{ nm}$) with high resistivity, as verified by STEM-EDX analyses. Finally, a top Al electrode ($\approx 125 \text{ nm}$) was intentionally defined by utilizing a conventional evaporation process ($0.5\text{--}1.5 \text{ \AA s}^{-1}$) that employed a shadow mask (to obtain strips of Al) to form Ohmic contact at the metal/oxide interface via the generation of a large number of oxygen vacancies.^[21]

Electrical Measurements: All electrical measurements were performed using a Keithley4200 semiconductor parameter analyzer with self-designed testing software under ambient conditions and without any encapsulation. A defined voltage bias was applied to the ITO bottom electrode while the Al top electrode remained grounded.

STEM-EDX Analysis: The ultrathin samples before and after 100 cycles of the I - V curve under 7 V STEM-EDX analysis were prepared using a focused ion beam (Hitachi FB-2100). The STEM-EDX analysis was performed using a JEM-ARM200F scanning transmission electron microscope and a JED-2300T analysis station operating at 200 kV . The line profiles of O were corrected by subtracting the background noise as determined from the Al electrode, whereas the Al profile was determined without any processing.

X-Ray Photoelectron Spectroscopy: The Al top electrode, which had a diameter of $1000 \mu\text{m}$, was cathodically or anodically polarized by sweeping the voltage over ranges of $0\text{--}7 \text{ V}$ or -7 to 7 V to create an unbalanced oxygen ion distribution. XPS (PHI Quantera II) was then performed on the bare surface of the polarized films after removing the Al electrode and AlO_x layers, which were precision stripped using epoxy resin.^[12] Binding energies of the core levels are calibrated against adventitious C1 s Peak (284.6 eV) in our case. The surface of the prepared film was checked using XPS to eliminate Al or AlO_x contaminants on the surface of ZnTPP films.

Computational Details: Our density functional calculations were performed using the Quantum Espresso (QE) package^[22] with norm-conserving pseudopotentials and generalized gradient approximation (GGA) exchange-correlation functionals parameterized by Perdew–Burke–Erzerhof (PBE).^[23] The initial molecular structures were taken as

the tetrabenzoporphyrin molecules.^[24] The “single porphyrin molecule in vacuum” geometry is simulated by constructing a simple tetragonal unit cell centered by the metal ions of the MTPP molecule. The size of the unit cell was selected such that spacings between molecules of adjacent images exceed 25 Bohr in all directions. The total energy of the systems was tested to converge within a 10^{-5} Rydberg window using this unit cell. A convergence criterion of 10^{-7} Rydberg was used for all self-consistency calculations. The molecular structures were relaxed until all of the force components were less than 10^{-4} Rydberg/Bohr. All calculations were performed at the Γ -point. We studied the oxygen ion adsorption mechanism on the metal centers of the ZnTPP, NiTPP, and CoTPP molecules. $E_{\text{Metal-O}}$ was calculated using

$$E_{\text{Metal-O}} = \left| E_{\text{molecule-O}} - E_{\text{molecule}} - \frac{1}{2} E_{\text{O}_2} \right| \quad (1)$$

where $E_{\text{molecule-O}}$, E_{molecule} , and E_{O_2} are total surface energies with one adsorbed oxygen ion, the porphyrin molecule, and the gas phase oxygen molecule, respectively. The $E_{\text{Metal-O}}$ and $L_{\text{Metal-O}}$ of the oxygen ion adsorptions on three different molecules are listed in Table S1 in the Supporting Information.

To overcome the underestimation of band gaps arising from conventional DFT calculations, G_0W_0 approximation was performed with the GWL code inside QE to calculate HOMO and LUMO energies of different MTPP species. A total of 2048 bands (94% unoccupied) were included to converge the calculation of the dielectric functions entering the screened interaction. Table S2 (Supporting Information) illustrates that the HOMO-LUMO gaps of all MTPP molecules were similar. The quantitative PBE underestimations of the gap were $\approx 40\text{--}50\%$. More accurate HOMO/LUMO positions were achieved using the G_0W_0 approximation.

Supporting Information

Supporting Information is available from the Wiley Online Library or from the author.

Acknowledgements

Z.Y.W., L.Y.W., and Y.M.W. contributed equally to this work. This research was supported by the National Natural Science Foundation of China (21774061, 21771135, 91833306, 51933005, 61775100, 61904150, 61905121, 61805203), Natural Science Foundation of Jiangsu Province, China (18KJA510003, BK20190734), Singapore Ministry of Education (MOE2017-T2-2-110), Agency for Science, Technology and Research (A*STAR) (Grant No. A1883c0011), National Research Foundation, Prime Minister's Office, Singapore under the NRF Investigatorship Programme (Award No. NRF-NRFI05-2019-0003), Synergetic Innovation Center for Organic Electronics and Information Displays, the Priority Academic Program Development of Jiangsu Higher Education Institutions (PAPD, YX03002), postdoctoral innovative talent support program (BX20180260), China postdoctoral science foundation (2018M64373), Shaanxi postdoctoral research grant program (2018BSHEDZZ115), and National Basic Research Program of China (973 Program) (2015CB932200).

Conflict of Interest

The authors declare no conflict of interest.

Data Availability Statement

Research data are not shared.

Keywords

metalloporphyrin/oxide memristor, neuromorphic computing, signal filtering, spike voltage-dependent plasticity

Received: June 8, 2021

Revised: July 25, 2021

Published online: September 12, 2021

- [1] a) A. Soltani, X. J. Wang, *Nat. Neurosci.* **2010**, *13*, 112; b) G. Indiveri, B. Linares-Barranco, R. Legenstein, G. Deligeorgis, T. Prodromakis, *Nanotechnology* **2013**, *24*, 384010; c) S. La Barbera, D. Vuillaume, F. Alibart, *ACS Nano* **2015**, *9*, 941; d) T. Kambe, R. Sakamoto, T. Kusamoto, T. Pal, N. Fukui, K. Hoshiko, T. Shimojima, Z. Wang, T. Hirahara, K. Ishizaka, S. Hasegawa, F. Liu, H. Nishihara, *J. Am. Chem. Soc.* **2014**, *136*, 14357; e) J. J. Yang, M. D. Pickett, X. Li, D. A. Ohlberg, D. R. Stewart, R. S. Williams, *Nat. Nanotechnol.* **2008**, *3*, 429; f) S. Kim, C. Du, P. Sheridan, W. Ma, S. Choi, W. D. Lu, *Nano Lett.* **2015**, *15*, 2203; g) S. Z. Li, F. Zeng, C. Chen, H. Y. Liu, G. S. Tang, S. Gao, C. Song, Y. S. Lin, F. Pan, D. Guo, *J. Mater. Chem. C* **2013**, *1*, 5292; h) M. D. Pickett, G. Medeiros-Ribeiro, R. S. Williams, *Nat. Mater.* **2013**, *12*, 114.
- [2] E. S. Fortune, G. J. Rose, *Trends Neurosci.* **2001**, *24*, 381.
- [3] P. Yao, H. Wu, B. Gao, J. Tang, Q. Zhang, W. Zhang, J. J. Yang, H. Qian, *Nature* **2020**, *577*, 641.
- [4] C. Li, M. Hu, Y. Li, H. Jiang, N. Ge, E. Montgomery, J. Zhang, W. Song, N. Dávila, C. E. Graves, Z. Li, J. P. Strachan, P. Lin, Z. Wang, M. Barnell, Q. Wu, R. S. Williams, J. J. Yang, Q. Xia, *Nat. Electron.* **2018**, *1*, 52.
- [5] M. L. Schneider, C. A. Donnelly, S. E. Russek, B. Baek, M. R. Pufall, P. F. Hopkins, P. D. Dresselhaus, S. P. Benz, W. H. Rippard, *Sci. Adv.* **2018**, *4*, e1701329.
- [6] G. Voglis, N. Tavernarakis, *EMBO Rep.* **2006**, *7*, 1104.
- [7] a) G. R. Yang, J. D. Murray, X.-J. Wang, *Nat. Commun.* **2016**, *7*, 12815; b) J. Zhao, B. Song, N. Xi, L. Sun, H. Chen, Y. Jia, *Automatica* **2014**, *50*, 1835.
- [8] a) L. D. Harmon, B. Julesz, *Science* **1973**, *180*, 1194; b) P. Yao, H. Wu, B. Gao, S. B. Eryilmaz, X. Huang, W. Zhang, Q. Zhang, N. Deng, L. Shi, H. S. P. Wong, H. Qian, *Nat. Commun.* **2017**, *8*, 15199.
- [9] M.-J. Lee, C. B. Lee, D. Lee, S. R. Lee, M. Chang, J. H. Hur, Y.-B. Kim, C.-J. Kim, D. H. Seo, S. Seo, U. I. Chung, I.-K. Yoo, K. Kim, *Nat. Mater.* **2011**, *10*, 625.
- [10] a) Z. Q. Wang, H. Y. Xu, X. H. Li, H. Yu, Y. C. Liu, X. J. Zhu, *Adv. Funct. Mater.* **2012**, *22*, 2759; b) J. J. Yang, M. D. Pickett, X. Li, D. A. A. Ohlberg, D. R. Stewart, R. S. Williams, *Nat. Nanotechnol.* **2008**, *3*, 429.
- [11] a) X.-F. Cheng, X. Hou, J. Zhou, B.-J. Gao, J.-H. He, H. Li, Q.-F. Xu, N.-J. Li, D.-Y. Chen, J.-M. Lu, *Small* **2018**, *14*, 1703667; b) M. Wang, S. Cai, C. Pan, C. Wang, X. Lian, Y. Zhuo, K. Xu, T. Cao, X. Pan, B. Wang, S.-J. Liang, J. J. Yang, P. Wang, F. Miao, *Nat. Electron.* **2018**, *1*, 130; c) X.-F. Cheng, W.-H. Qian, J. Wang, C. Yu, J.-H. He, H. Li, Q.-F. Xu, D.-Y. Chen, N.-J. Li, J.-M. Lu, *Small* **2019**, *15*, 1905731.
- [12] Y. Aoki, C. Wiemann, V. Feyer, H.-S. Kim, C. M. Schneider, H. Ill-Yoo, M. Martin, *Nat. Commun.* **2014**, *5*, 3473.
- [13] a) J. Park, S. Lee, J. Lee, K. Yong, *Adv. Mater.* **2013**, *25*, 6423; b) S. Baek, J. Song, S. Lim, *Phys. B* **2007**, *399*, 101.
- [14] a) W. E. Kaden, T. Wu, W. A. Kunkel, S. L. Anderson, *Science* **2009**, *326*, 826; b) M. Prezioso, F. Merrikh-Bayat, B. D. Hoskins, G. C. Adam, K. K. Likharev, D. B. Strukov, *Nature* **2015**, *521*, 61; c) C. Du, W. Ma, T. Chang, P. Sheridan, W. D. Lu, *Adv. Funct. Mater.* **2015**, *25*, 4290.
- [15] a) T. B. Bentley, H. Meng, R. N. Pittman, *Am. J. Physiol.: Heart Circ. Physiol.* **1993**, *264*, H1825; b) I. W. M. Smith, *Chem. Soc. Rev.* **2008**, *37*, 812.
- [16] M. Hansen, M. Ziegler, L. Kolberg, R. Soni, S. Dirkmann, T. Mussenbrock, H. Kohlstedt, *Sci. Rep.-Uk* **2015**, *5*, 13753.
- [17] M. Hansen, M. Ziegler, L. Kolberg, R. Soni, S. Dirkmann, T. Mussenbrock, H. Kohlstedt, *Sci. Rep.* **2015**, *5*, 13753.
- [18] J. Liu, Z. Yin, X. Cao, F. Zhao, Z. Yin, A. Lin, L. Xie, Q. Fan, F. Boey, H. Zhang, W. Huang, *ACS Nano* **2010**, *4*, 3987.
- [19] W. Badenhurst, T. Hanekom, J. J. Hanekom, *Biol. Cybern.* **2016**, *110*, 403.
- [20] a) L. Ma, S. Pyo, J. Ouyang, Q. Xu, Y. Yang, *Appl. Phys. Lett.* **2003**, *82*, 1419; b) J. Ying, J. Han, L. Xiang, W. Wang, W. Xie, *Curr. Appl. Phys.* **2015**, *15*, 770.
- [21] J. J. Yang, J. P. Strachan, F. Miao, M.-X. Zhang, M. D. Pickett, W. Yi, D. A. A. Ohlberg, G. Medeiros-Ribeiro, R. S. Williams, *Appl. Phys. A* **2011**, *102*, 785.
- [22] P. Giannozzi, S. Baroni, N. Bonini, M. Calandra, R. Car, C. Cavazzoni, D. Ceresoli, G. L. Chiarotti, M. Cococcioni, I. Dabo, A. Dal Corso, S. de Gironcoli, S. Fabris, G. Fratesi, R. Gebauer, U. Gerstmann, C. Gougoussis, A. Kokalj, M. Lazzeri, L. Martin-Samos, N. Marzari, F. Mauri, R. Mazzarello, S. Paolini, A. Pasquarello, L. Paulatto, C. Sbraccia, S. Scandolo, G. Sclauzero, A. P. Seitsonen, A. Smogunov, P. Umari, R. M. Wentzcovitch, *J. Phys.: Condens. Matter* **2009**, *21*, 395502.
- [23] J. P. Perdew, K. Burke, M. Ernzerhof, *Phys. Rev. Lett.* **1996**, *77*, 3865.
- [24] R. R. Valiev, V. N. Cherepanov, V. Y. Artyukhov, D. Sundholm, *Phys. Chem. Chem. Phys.* **2012**, *14*, 11508.